nature astronomy

Article

https://doi.org/10.1038/s41550-025-02500-2

A giant disk galaxy two billion years after the Big Bang

Received: 23 December 2024

Accepted: 4 February 2025

Published online: 17 March 2025

Check for updates

Weichen Wang[1] ✉, Sebastiano Cantalupo[1], Antonio Pensabene[1], Marta Galbiati[1], Andrea Travascio[1], Charles C. Steidel[2], Michael V. Maseda[3], Gabriele Pezzulli[4], Stephanie de Beer[1], Matteo Fossati[1,5], Michele Fumagalli[1,6], Sofia G. Gallego[7], Titouan Lazeyras[1], Ruari Mackenzie[8], Jorryt Matthee[9], Themiya Nanayakkara[10] & Giada Quadri[1]

Observational studies have shown that galaxy disks were already in place in the first few billion years of the Universe. The early disks detected so far, with typical half-light radii of 3 kpc at stellar masses around $10^{11}\,M_{\odot}$ for redshift $z \approx 3$, are significantly smaller than today's disks with similar masses, which is in agreement with expectations from current galaxy models. Here we report observations of a giant disk at $z = 3.25$, when the Universe was only two billion years old, with a half-light radius of 9.6 kpc and stellar mass of $3.7^{+2.6}_{-2.2} \times 10^{11}\,M_{\odot}$. This galaxy is larger than any other kinematically confirmed disks at similar epochs and is surprisingly similar to today's largest disks with regard to size and mass. James Webb Space Telescope imaging and spectroscopy reveal its spiral morphology and a rotational velocity consistent with a local Tully–Fisher relationship. Multiwavelength observations show that it lies in an exceptionally dense environment, where the galaxy number density is more than ten times higher than the cosmic average and mergers are frequent. The discovery of such a giant disk suggests the presence of favourable physical conditions for large-disk formation in dense environments in the early Universe, which may include efficient accretion of gas carrying coherent angular momentum and non-destructive mergers between exceptionally gas-rich progenitor galaxies.

The galaxy, dubbed the 'Big Wheel', was discovered serendipitously in a bright-quasar field at redshift (z) of 3.25 (refs. 1,2) through James Webb Space Telescope (JWST) imaging at wavelengths of 1.5 μm and 3.2 μm (rest-frame 0.4 μm and 0.8 μm). Hubble Space Telescope (HST) observations at 0.8 μm (rest-frame 0.2 μm) reveal only isolated clumps at the galaxy outskirts, possibly tracing young stars and/or low dust obscuration. A red, green, blue image combining the HST and JWST images is shown in Fig. 1b, and Fig. 1a shows a zoomed-in view of the Big Wheel. The Big Wheel features a red centre, which is visible only in the JWST near-infrared filters (green and red channels; see also Extended Data Fig. 1), and a stellar disk extending to at least 30 kpc in diameter. Spiral-arm features are visible, appearing clumpy in rest-frame ultraviolet, reminiscent of some spiral galaxies at $z \approx 0$ (ref. 3). Its stellar half-light radius is 9.6 kpc along the major axis in the rest-frame optical (0.5 μm), as measured using statmorph[4] (Methods).

Hydrogen Hα spectroscopy obtained with the Near-Infrared Spectrograph (NIRSpec) confirms the rotating-disk nature of Big Wheel. Three spectroscopic slits (Methods) were placed onto the

[1]Department of Physics, Universita degli Studi di Milano-Bicocca, Milano, Italy. [2]Cahill Center for Astronomy and Astrophysics, California Institute of Technology, Pasadena, CA, USA. [3]Department of Astronomy, University of Wisconsin-Madison, Madison, WI, USA. [4]Kapteyn Astronomical Institute, University of Groningen, Groningen, The Netherlands. [5]INAF - Osservatorio Astronomico di Brera, Merate (LC), Italy. [6]INAF - Osservatorio Astronomico di Trieste, Trieste, Italy. [7]Astroparticle and Cosmology Laboratory, Université Paris Cité, Paris, France. [8]Department of Physics, ETH Zürich, Zürich, Switzerland. [9]Institute of Science and Technology Austria (ISTA), Klosterneuburg, Austria. [10]Centre for Astrophysics and Supercomputing, Swinburne University of Technology, Hawthorn, Australia. ✉e-mail: weichen.wang@unimib.it

https://doi.org/10.1038/s41550-025-02500-2

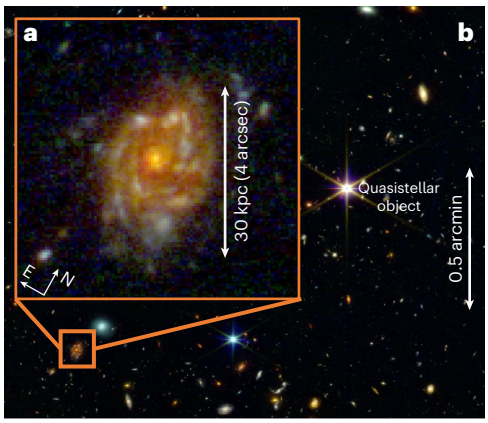

Fig. 1 | Composite false-colour images of the Big Wheel galaxy at $z = 3.245$. **a**,**b**, The galaxy shows a red and compact centre and a giant stellar disk extending to at least 30 kpc in diameter. The disk appears clumpy with manifest spiral structures (**a**). The Big Wheel is located about 70 arcsec away (about 0.5 pMpc) from a bright quasar at a similar redshift (**b**). The quasar was originally chosen as the centre of the observation field. This region shows an exceptionally high galaxy number density compared with the cosmic average. The filters used to create the colour image are HST F814W (0.8 µm, blue), JWST F150W2 (1.5 µm, green) and JWST F322W2 (3.2 µm, red). The disk is visible in the green and red channels but not in the blue channel.

galaxy (Fig. 2a–c), including one covering the galaxy centre. Hα two-dimensional spectra are presented in Fig. 2d–f, whereas the corresponding slit positions are indicated in Fig. 2a–c. Initial evidence supporting disk rotation can be gleaned from the slit spectrum covering the galaxy centre (Fig. 2d). Moving towards the external regions, the velocity increases first and then plateaus at around ±200 km s^{-1} (before inclination correction). Such a pattern is typical of disk galaxies with flat rotation curves[5]. Additional features are present in the spectra, such as a bright clump that appears kinematically distinct from the disk (green box) and could be associated with a companion galaxy seen in projection.

The Hα spectra of the remaining slits (Fig. 2e–f) also have patterns consistent with disk-like rotation. To demonstrate this, we measured the rotation velocities from the Hα profiles across the slits, as shown in Fig. 2d–f (Methods and Extended Data Fig. 2) and we present the result as a velocity map in Fig. 2g. As shown in Fig. 2d–f, these profiles agree remarkably well over the main stellar disk body with predictions from a simple disk kinematic model, in which a flat rotation curve is adopted (yellow curves in Fig. 2d–f).

The disk model, described in detail in the Methods, includes six free parameters that specify the location and velocity of the disk centre, major axis orientation and normalizations of the rotation curve. The model was fit to the data using the Markov Chain Monte Carlo scheme emcee[6]. The best-fit model is presented in Fig. 2h and the residuals are shown in Fig. 2i. The maximum rotation velocity (corrected for inclination) $v_{\rm rot}$ is 331^{+30}_{-30} km s^{-1}, that is, $5.4^{+1.6}_{-1.2}$ times the velocity dispersion $\sigma_{\rm int}$ (61^{+17}_{-13} km s^{-1}; Methods). These values indicate that the Big Wheel is rotationally supported and has a dispersion value consistent with (smaller) turbulent disks at similar and lower redshifts[7–9]. Combining $v_{\rm rot}$ and $\sigma_{\rm int}$ using the commonly adopted relationship in the literature[10] (Methods), we obtained a circular velocity $v_{\rm circ} = 352^{+30}_{-30}$ km s^{-1}. The velocity map of the molecular gas obtained through Atacama Large (sub-)Millimeter Array (ALMA) observations[1] covering the full galaxy, albeit with lower spatial resolution, shows consistent results (Extended Data Figs. 3 and 4 and Methods).

The stellar mass and star formation rate (SFR) were obtained by fitting the photometry in seven filters against spectral energy distribution (SED) models with the Prospector tool[11] (Extended Data Fig. 5 and Methods). Flexible star formation histories (SFHs) and dust attenuation laws were adopted, as well as the potential emission from an active galactic nucleus (AGN) (Extended Data Fig. 6). The best-fit stellar mass and SFR values are $3.7^{+2.6}_{-2.2} \times 10^{11}\,M_\odot$ and $2.5^{+7.5}_{-2.1} \times 10^{2}\,M_\odot$ yr^{-1}, respectively. These results indicate that the Big Wheel is one of the most massive systems detected so far at $z \gtrsim 3$, some of which were discovered only recently with JWST[12].

The physical properties of the Big Wheel are summarized in Table 1 and are compared with the observed galaxy population at similar redshifts in Fig. 3. Most intriguingly, the Big Wheel has a larger radius (measured at rest-frame 0.5 µm) and is more massive than any other kinematically confirmed disk galaxy discovered so far at similar redshifts (Fig. 3a and Methods). Figure 3b shows the size versus stellar mass relationships for $z \approx 3$ star-forming galaxies for both observations and simulations, as well as the observed relationship at $z \approx 0$. The Big Wheel is clearly offset to high values, both in terms of stellar mass and sizes, with respect to both the observed and simulated relationships at $z \approx 3$.

In addition, in terms of size, the Big Wheel galaxy is more similar to $z \approx 0$ disk galaxies than other currently known disk galaxies at $z \approx 3$. As shown in Fig. 3d, it is located on top of the stellar mass Tully–Fisher relationship of the $z \approx 0$ disks[5] with a stellar mass and circular velocity similar to local 'super-spirals'[13,14]. Despite the similarities to the $z \approx 0$ objects, the Big Wheel galaxy is actively growing in mass like other galaxies at $z \approx 3$, with an SFR consistent with the trend of typical $z \approx 3$ star-forming galaxies (Fig. 3c).

Our observations reveal that the Big Wheel is a giant rotating disk with physical properties unique for $z \approx 3$, which raises questions about its formation scenario. Within the classical theoretical framework[15,16], the disk size is expected to be simply proportional to the halo size multiplied by the dimensionless halo spin parameter (λ) (refs. 15,16), with small deviations with halo concentration and disk-to-halo mass ratio. The halo λ follows a distribution that is well constrained from simulations and can be fitted with a log-normal function with an average of ~0.035 and a log-normal standard deviation (in log base 10) of ~0.25 (refs. 16,17) without significant variations with halo mass and redshift[17,18].

Despite the model simplicity, its predictions are consistent with the observed galaxy size distributions both in terms of shape and scatter. In particular, the most recent observations at $z \approx 3$, find a log-normal size distribution with an intrinsic scatter of ~0.22–0.28 (refs. 19,20), which is strikingly similar to the simple expectations mentioned. As shown in Fig. 3b, the Big Wheel is at least three times larger than the expected size of star-forming, disk galaxies at its mass and redshift given the observed size–mass relationship in random fields[19,20]. The probability of randomly finding such a galaxy, if environment does not play a role, is less than 2% (see Methods for details). The Big Wheel is one of the few star-forming galaxies with rest-frame optical size measurement and a mass above $10^{11}\,M_\odot$ found so far at $z > 3$, and the only one with confirmed kinematical measurements demonstrating its rotating disk nature. As such, its serendipitous discovery in one of the largest overdensities of galaxies found so far at $z \gtrsim 3$ (refs. 1,2) suggests that additional physical mechanisms could be at play in determining the size of massive disk galaxies in such regions of the Universe.

Major mergers are expected to be more frequent than the cosmic average in overdense regions[21] and a few models suggest that they can, in exceptional conditions, facilitate disk growth by increasing the disk spin rather than destroying it[22,23]. In particular, models suggest that disks can survive disruption or reform afterwards if mergers have favourable orbital parameters and the progenitor galaxies are gas rich[22,23]. If these predictions are correct, the presence of such a giant disk in a large overdensity of galaxies could imply, for example, a connection between the dense environment and an elevation of the gas fraction of galaxies. In turn, the high gas content of galaxies could be caused by more efficient accretion of the gas from the cosmic web in denser environments at early cosmic epochs.

https://doi.org/10.1038/s41550-025-02500-2

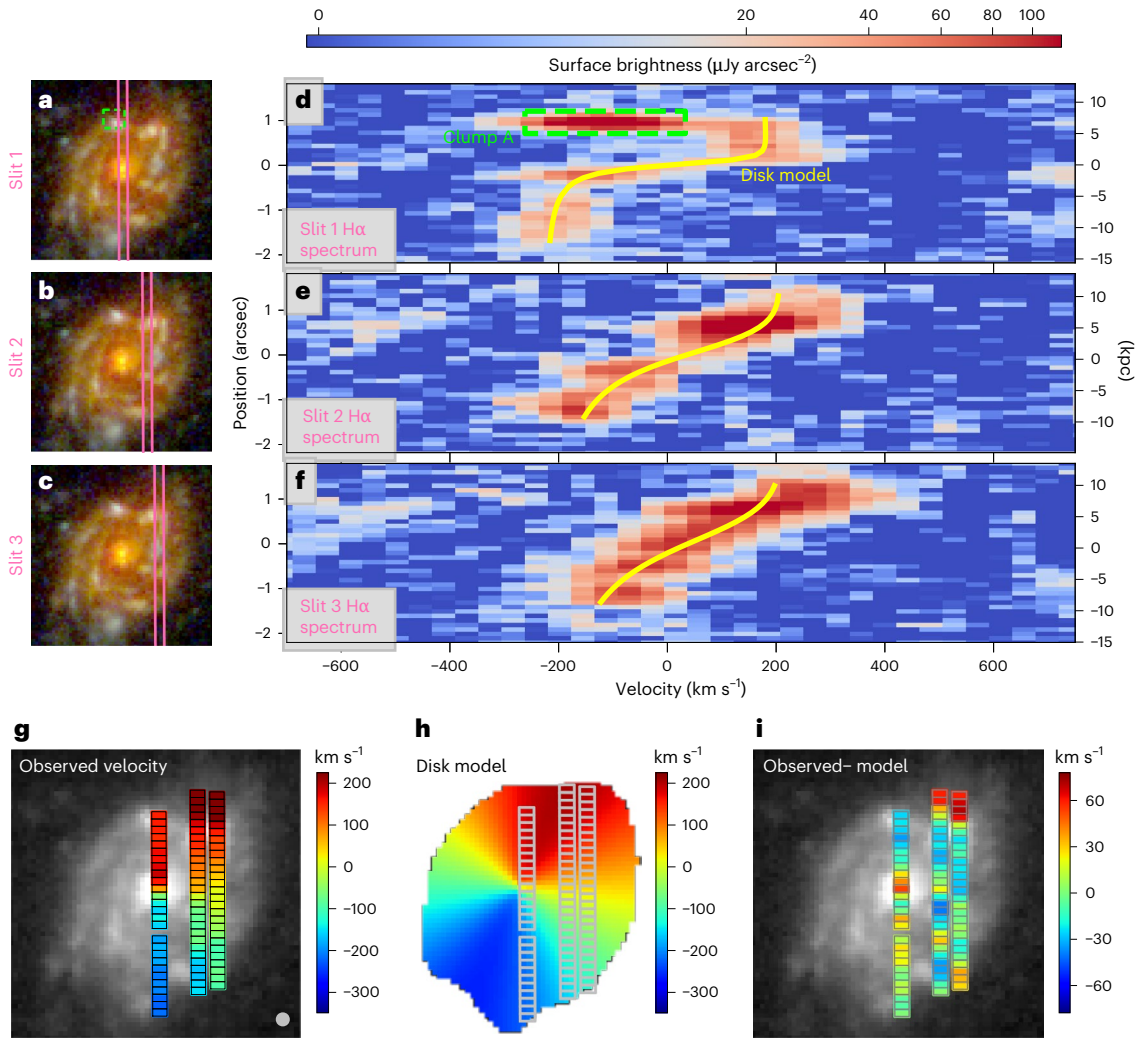

Fig. 2 | JWST kinematic measurements supporting the rotating-disk nature of the Big Wheel. a–c, The spectral slits used in the observations, slit 1 (**a**), slit 2 (**b**) and slit 3 (**c**). **d–f**, Two-dimensional spectra obtained from slit 1 (**d**), slit 2 (**e**) and slit 3 (**f**). The panels in **a–c** are aligned with these spectra along the *y* direction. The two-dimensional spectra are continuum-subtracted and centred on the Hα emission line, where the *x* axis is the dispersion direction indicating the line-of-sight velocity and the *y* axis indicates the spatial position along the slit. The yellow curve overlaid on each spectrum represents the ridge-line of the Hα profile predicted by a simple disk model. **g–i**, Velocity map (**g**) obtained by measuring the centroids of the Hα profiles across the three slits, excluding a clump with peculiar morphology and kinematics (green box) and a region without Hα detection in slit 1. The map from observations is in agreement with the disk model (**h**) with no significant residuals over the main stellar disk body (**i**). Small residuals (~30–60 km s^{-1}) in the kinematics are only present at the upper ends of slits 2 and 3, at the edge or outside the stellar disk (**i**). The spatial resolution of the observations is indicated at the bottom right of **g**.

Alternatively, large disks could also be the result of accretion of cosmic gas with coherent angular momentum, resulting in a larger disk-to-halo angular momentum ratio with respect to expectations from previous analytical models[24].

The relevant galaxy formation and evolution mechanisms are still not well constrained to date. To the best of our knowledge, current cosmological simulations[25,26], some of which are presented in Fig. 3, have not predicted disks as large as the Big Wheel galaxy at $z \gtrsim 3$ at comparable masses.

In addition to its uncertain origin, the subsequent evolution of the Big Wheel also remains unknown. The fact that the galaxy is not growing in isolation and the presence of at least one companion galaxy, as shown in Fig. 2, could suggest future mergers responsible for an evolution in the Big Wheel properties.

Moreover, its dense environment suggesting the presence of a proto-cluster[1,2] hints that its descendant might be one of the most massive members of today's galaxy clusters. Nevertheless, further studies are needed to understand how common giant disks such as the Big Wheel were in dense environments at early cosmic epochs and whether their physical properties and number densities are consistent with the putative progenitors of today's most massive cluster galaxies.

Methods

Imaging observations and data reduction

Imaging data were obtained from HST General Observer programme 17065 (principal investigator (PI), Cantalupo) and JWST General Observer programme 1835 (PI, Cantalupo) using the NIRCam filters, F150W2 and F322W2, each for 1,632 s of exposure, and HST filters ACS/WFC F625W and ACS/WFC F814W, for 10 and 12 orbits, respectively. The JWST data were reduced and combined using the official JWST pipeline (v.1.9.3 (ref. 27)) with calibration reference file version jwst_1039.pmap. We implemented customized steps in the reduction to remove the correlated readout noises and stray light, following the practices adopted among the literature[28]. The image resolutions in terms of the full-width at half-maximum (FWHM) were 0.12 arcsec, 0.12 arcsec, 0.05 arcsec and 0.11 arcsec for F625W, F814W, F155W2 and F322W2, respectively.

https://doi.org/10.1038/s41550-025-02500-2

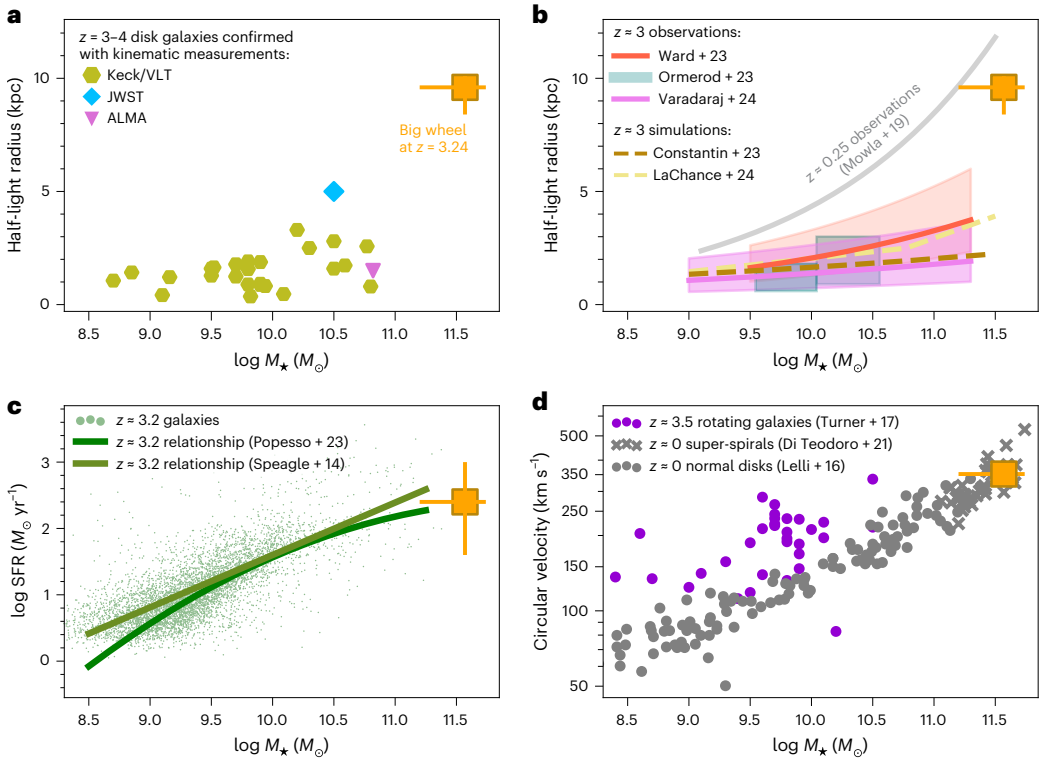

Fig. 3 | Physical properties of the Big Wheel. a–d, The Big Wheel galaxy, at $z = 3.245$, is larger and more massive than any other kinematically confirmed disk galaxy discovered to date at similar redshifts (**a**). It is well above the extrapolation of the size–mass relationship at a mass of $10^{11.5}\,M_\odot$ and $z \approx 3$ from observations and simulations, and is more consistent with the size of $z \approx 0$ galaxies (**b**). Furthermore, it follows the Tully–Fisher relationship (circular velocity versus stellar mass) of the disk galaxies at $z \approx 0$ (**d**). The Big Wheel has an SFR consistent with the (extrapolated) trend with stellar mass for typical star-forming galaxies at $z \approx 3$ (**c**). Error bars of the stellar mass, radius, SFR and circular velocity take into account both random and systematic uncertainties, which are described in the Methods. Details of the literature studies included here are also provided in the Methods.

We also obtained near-infrared data with the Very Large Telescope (VLT) in 2022 as part of a programme in P110 (PI: Cantalupo). The High Acuity Wide field K-band Imager (HAWKI) was used in the ground layer adaptive optics mode, leading to spatial resolutions of 0.4 arcsec in FWHM, using the filters CH4, H and Ks. On-source exposure times were 60 min, 100 min and 100 min, respectively. The images of each filter were reduced and combined using the official pipeline EsoRex[29].

Photometry was performed on the images described above using the Source Extractor tool[30]. For the measurement, the image mosaics were resampled to a common grid of 0.06 × 0.06 arcsec pixels using the drizzle package[31]. Source Extractor was run in dual mode for the space-based and ground-based data, using the F322W2 and H mosaics, respectively, as detection images.

Spectroscopic observations and data reduction

Follow-up spectroscopic observations using NIRSpec were obtained as a part of the same JWST programme as above. The observations used the Micro-Shutter Assembly (MSA), with the F170LP/G235H filter and grating pair, leading to a resolving power of $R \approx 3{,}200$ or, equivalently, 95 km s^{-1} in FWHM at the observed wavelength of the Hα line (2.8 μm). The exposure time was ~3 h for each of the three MSA slits. The data for each slit were reduced and combined using the official JWST pipeline (v.1.11.3) with calibration reference file version jwst_1097.pmap. The spatial resolution of the data, which was inferred with the WEBBPSF tool[32], was 0.13 arcsec in FWHM at 2.8 μm and was resampled to a pixel scale of 0.10 arcsec. The smooth background and galaxy continua were removed by applying a median filter with a width of 3,000 km s^{-1} to each pixel row of the two-dimensional spectra and subtracting the filtered product from the original spectra. We also extracted an integrated one-dimensional spectrum from the combined two-dimensional spectra. The resulting one-dimensional spectrum and identified emission lines are shown in Extended Data Fig. 6a. The galaxy redshift was inferred from the observed wavelengths of the Hα, [N II] and Hβ lines on the spectrum.

The Big Wheel was also observed with ALMA in Cycle 8 (identification number (ID), 2021.1.00793.S; PI, Cantalupo), the details of which are provided in ref. 1. Data cleaning was performed down to 1.5σ with a circular mask of 2" in radius, which enclosed emission of the galaxy in the cube. The synthesized beam size (FWHM) of the 'cleaned' data cube was 1.4" × 1.3" at 109.00 GHz. We fitted the spectral continua with zeroth-order polynomials and subtracted them from the cube using the task imcontsub of Common Astronomy Software Application[33].

The Big Wheel was also observed using the Advanced CCD Imaging Spectrometer onboard the Chandra X-ray Observatory during 2022–2023 (PI, Cantalupo), with a total of 634 ks of exposure. The galaxy is associated with a 3σ X-ray point source with a luminosity of $L_{2-10\,\mathrm{keV}} = 9.8^{+1.8}_{-1.7} \times 10^{43}$ erg s^{-1}, which was measured assuming a photon index of 1.7–1.8 and corrected for absorption[34]. Such a luminosity is consistent with the typical value of a moderate-luminosity Seyfert AGN[35]. The existence of the AGN was also confirmed from the ratios of the nebular emission lines from the galaxy centre ($r < 1.5$ kpc) on the NIRSpec spectrum, according to the criteria in refs. 36,37, whereas the emission lines from all other parts of the galaxy are consistent with being driven by star formation (Extended Data Fig. 6b).

Galaxy size measurements

The half-light radius in the rest-frame optical was measured from the background-subtracted images in the NIRCam F150W2 and F322W2 filters. The galaxy images in these filters, as well as the F814W image, are shown in Extended Data Fig. 1. We measured the radius by running a

https://doi.org/10.1038/s41550-025-02500-2

Table 1 | Properties of the Big Wheel galaxy

Property	Value	Unit
Right ascension (J2000)	00 h 41 min 35.113 s	–
Declination (J2000)	−49° 37′ 12.42″	–
z[a]	3.2452	–
Stellar mass (adopted value)[b]	$3.7^{+2.6}_{-2.2} \times 10^{11}$	Solar mass ($M_\odot$)
Stellar mass (inferred with a parametric SFH)[c]	$2.3^{+1.4}_{-0.9} \times 10^{11}$	Solar mass ($M_\odot$)
SFR[b]	$2.5^{+7.5}_{-2.1} \times 10^{2}$	$M_\odot\,yr^{-1}$
Half-light radius[d]	$1.27^{+0.07}_{-0.16}$, $9.6^{+0.5}_{-1.2}$	Arcsec, kiloparsec
Minor-to-major axis ratio	$0.72^{+0.04}_{-0.04}$	–
Disk inclination angle[e]	44^{+3}_{-4}	Degree
v_{rot}[f]	331^{+30}_{-30}	km s
σ_{int}	61^{+17}_{-13}	km s^{-1}
v_{rot}/σ_{int}	$5.4^{+1.6}_{-1.2}$	–
v_{circ}[f]	352^{+30}_{-30}	km s^{-1}
Disk position angle (kinematics)[g]	19^{+4}_{-4}	Degree
Disk position angle (morphology)[g]	10^{+1}_{-1}	Degree
CO(4–3) line luminosity	1.3×10^{8}	Solar luminosity ($L_\odot$)
H_2 mass estimated from CO	$1.8^{+1.0}_{-0.8} \times 10^{11}$	$M_\odot$
Environment overdensity[h]	≥10	–

[a]Measured from the Hα and [N II] emission lines. [b]Values inferred from SED fitting with a non-parametric SFH using Prospector[11] and adopted in this work. The SFR was calculated from a 100 Myr timescale. [c]Inferred using an alternative parametric form of SFH for reference. See Methods and ref. 2 for details. [d]Measured along the major axis of the galaxy at rest-frame 0.5 µm. [e]Angle between the galaxy disk plane and sky plane, with 0° indicating fully face-on; inferred from the axis ratio and ellipticity measurements. [f]See Methods for details regarding the definition of the two quantities. [g]Orientation angle of the disk major axis projected on the sky plane, inferred from the Hα kinematics and galaxy morphology, respectively. North (east) corresponds to 0° (90°). [h]Inferred from galaxy number density measurements as described in ref. 1.

non-parametric morphological analysis using statmorph[4]. This method is free from any assumption regarding the functional form of the galaxy light profile. The radius measurements were made for both the F150W2 and F322W2 filters. For each filter, we measured the radius of an ellipse enclosing half of the total light of the galaxy. Throughout the measurement, the radius was measured along the major axis of the ellipse and the orientation and ellipticity of the ellipse were fixed to values calculated from the mathematical moments of the pixel flux density distribution, which, in turn, were physically determined by the global morphology of the galaxy (see refs. 4,30 for details). The half-light radii measured from the two filters were 1.34 arcsec and 1.12 arcsec, respectively. As a check for consistency, we also measured the radius by fitting the Sérsic[38] profiles with statmorph using the point spread functions (PSFs) measured from stars in the field. The resulting half-light radii were all within 5% of the values reported above. Masking out clump A in Fig. 2a, which might be a companion galaxy, led to only negligible (<2%) changes in measured sizes.

The radial light profiles, measured along the galaxy major axis, are shown in Supplementary Fig. 1a, together with exponential disk profiles for comparison. Both the F150W2 and F322W2 profiles are consistent with exponential disks with deviations in the central regions, which are, at least, partially due to the diffuse dust attenuation (Supplementary Fig. 1b) as corroborated by the smoother dust-corrected mass density profile shown in Supplementary Fig. 1c. The Hα attenuation inferred from the Hα-to-Hβ ratios following ref. 39 is also shown for reference, but we caution that it may be subject to NIRSpec flux calibration errors[40] and traces only sightlines towards the youngest stars, which does not reflect attenuation to the full continuum light seen in the two broad filters[41,42]. We evaluated the uncertainties of the size measurements, which could be caused by beam-smearing effects due to the finite PSF of the imaging data and the imaging noise. To quantify the effects, we created a model exponential disk with an intrinsic half-light radius of 1 arcsec, convolved the model image with the NIRCam PSF and added artificial noise to the image. Then, we measured the half-light radius from this synthetic image in the same way as for the real data. For each filter, such a series of steps was repeated 500 times, from which a distribution of the measured radii was obtained. From the distribution, we found that the measured sizes deviate from the intrinsic value (1 arcsec) by only 2.8% and 3.4% for F150W2 and F322W2 at the 3σ confidence level, which indicates that the uncertainties due to beam smearing and noises are relatively small. These percentage values were adopted as the relative uncertainties of our size measurements.

In addition, we investigated whether the Big Wheel is subject to any gravitational lensing magnification caused by any foreground (that is, low redshift) nearby galaxy or galaxy cluster. This possibility was rejected based on the non-detection of any foreground cluster according to the X-ray and galaxy redshift measurements available to the field and the non-detection of any galaxy nearby with a mass large enough for lensing.

Finally, following the convention adopted in the literature[19,43,44], we inferred the half-light radius of the Big Wheel galaxy at rest-frame 0.5 µm. It was calculated by interpolating between the radius values measured in the two NIRCam filters, under the assumption that the radius is a linear function of wavelength. To account for the systematic uncertainty due to the interpolation conservatively, we adopted the sizes measured in the two individual filters as the bounds of the uncertainty range and then combined in quadrature this uncertainty with the propagated uncertainty due to the beam smearing and noise. The final calculated half-light radius was $1.27^{+0.07}_{-0.16}$ arcsec or, equivalently, $9.6^{+0.5}_{-1.2}$ kpc.

Kinematic analysis and modelling

One-dimensional Hα kinematical profiles were obtained from the two-dimensional spectra from each pixel row, which spanned 0.1 arcsec along the slit, after convolving them with the instrument line spread function. The one-dimensional spectra were then fit with a Gaussian using emcee[6]. Outputs of the fits include the rotation velocity (Gaussian centroid) and velocity dispersion (Gaussian width) as a function of the spatial location along the slit, which are shown in Extended Data Fig. 2. Using the rotation velocities measured from the three slits, we created a velocity map of the galaxy (Fig. 2g).

For the disk modelling, we adopted a flat rotation curve using the galpy Python package[45]. The rotation curve model had a form corresponding to the commonly used pseudo-isothermal potential[46]. It has two free parameters determining the location where the rotation curve turns flat and the plateau velocity, respectively. We created a model galaxy disk using this rotation curve, with the disk inclination angle fixed to that inferred from the disk ellipticity in F322W2, and the orientation angle in the sky plane and central velocity of the disk as two free parameters. Two other free parameters are included which anchored the galaxy centre (x, y). Then, we created a velocity map from this six-parameter disk model by calculating the velocity along the line of sight for each part of the disk. The model map was fitted against the observed velocity map using emcee. After the fitting was complete, we calculated the 50th percentiles of the parameter posterior distributions and used these parameters to create the best-fit disk model.

Based on the measurements and modelling, we derived the following galaxy kinematic properties. First, we calculated the v_{rot}, defined as the maximum rotation velocity after inclination correction at one half-light radius, where the rotation curve flattens. We calculated the

16–84th percentiles of the v_{rot} posterior as the 1σ uncertainty from fitting. In addition, wiggles and other small variations from perfect rotating-disk motion are seen in the velocity profiles in Extended Data Fig. 2. Such features are comparable to the ones commonly seen in other disk galaxies in the local Universe, including apparently isolated sources (for example, refs. 47–50) and they might also contribute to the uncertainty as a systematic term. To quantify this, we calculated the mean absolute deviation of the observed rotation curve with respect to the model (deprojected for inclination) and used it as an upper limit for the systematic uncertainty, which was then combined with the fitting uncertainty as the full uncertainty of v_{rot}. Second, we measured the averaged intrinsic velocity dispersion σ_{int} as the median of the dispersion values measured from the two off-centre slits in Extended Data Fig. 2b,c, where the beam-smearing effect was expected to be minimal (see below). The 16th and 84th percentiles of the dispersion values in Extended Data Fig. 2b,c are quoted as the 1σ uncertainty range. The values of v_{rot} and σ_{int} are listed in Table 1. Finally, we calculated the circular velocity v_{circ}, which is used in Fig. 3d, using the following relationship adopted in refs. 9,10: $v_{circ}^2 = v_{rot}^2 + 2 \times 1.68\,(R/R_{eff})\,\sigma_{int}^2$, in which R is where v_{rot} was measured in terms of radial distance and is equal to one effective radius (R_{eff}) for the Big Wheel galaxy. The calculated value of v_{circ} was 352^{+30}_{-30} km s^{-1}.

We investigated the effect of the finite spatial resolution of the observations on the modelling described above, namely, the beam-smearing effect[51]. We found that it had no substantial impact on the kinematic measurements because the NIRSpec spatial resolution element (0.13 arcsec) was substantially smaller than the galaxy size. To justify this, we created a model galaxy with an exponential two-dimensional flux density profile and an intrinsic velocity map identical to what is shown in Fig. 2h. We created a three-dimensional mock cube of the intrinsic Hα line emission based on this set-up. Next, we convolved each wavelength slice of this cube by the instrument PSF to get the synthetic cube 'seen' at the JWST resolution and produced the corresponding velocity map. We found that this map deviated from the intrinsic velocity map by no more than 15 km s^{-1}, except for the region within 0.2 arcsec of the centre, confirming that the beam-smearing effect has negligible impact for most parts of the galaxy.

The CO velocity map of the Big Wheel galaxy from the ALMA observations was obtained through the first moments of the CO(4–3) profiles. The map is shown in Extended Data Fig. 3a, and the Hα velocity map is shown in Extended Data Fig. 3b for comparison. The CO map has a substantially larger PSF than the Hα map and, as a result, shows narrower spans of velocity owing to the stronger beam-smearing effect[51]. Nevertheless, the CO map shows smooth velocity gradients oriented along the galaxy major axis similarly to the Hα, which provides evidence that both the cold molecular and warm ionized gases rotate in a similar fashion. The observed CO kinematics is quantitatively consistent with the Hα kinematics when the ALMA PSF is taken into account, as shown in Extended Data Fig. 4. In addition, the gas mass was measured from the ALMA data and is listed in Table 1. It was obtained using the CO-to-H_2 conversion factors described in ref. 1.

Stellar mass and SFR measurements

The stellar mass and SFR were measured from SED fits with the Prospector tool[11,52]. Photometric flux densities measured from seven filters were used in the fit: ACS F625W, ACS F814W, NIRCam F150W2, HAWKI CH4, HAWKI H, HAWKI Ks and NIRCam F322W2. The measured flux densities and the corresponding best-fit SED model are presented in Extended Data Fig. 5. For the fitting, we fixed the redshift to the value measured from the NIRSpec spectrum. A non-parametric form of the SFH with a prior favouring continuity[53] was adopted, binned into seven consecutive ranges in look-back time: 0–50 Myr, 50–100 Myr, 100–150 Myr, 150–200 Myr, 200–400 Myr, 400–800 Myr and 800–1,900 Myr. A Chabrier[54] initial mass function (IMF) and a Charlot and Fall[55] flexible dust attenuation law were adopted. A log-uniform prior was adopted for the stellar mass, a truncated normal prior was adopted for the optical depth of dust, a uniform prior was adopted for the power-law index of the dust attenuation law and a log-uniform prior was applied for the stellar metallicity, identical to those adopted in ref. 53. Emission from the AGN was also modelled following the prescription described in ref. 53, although the relevant parameters were unconstrained by the fit. The total stellar mass and SFR (averaged over 100 Myr) of the galaxy were calculated as the 50th percentiles of the Bayesian posteriors. The uncertainties were calculated from the 5–95th percentiles of the posteriors and added in quadrature with the systematic uncertainties due to the fitting assumptions as quantified by ref. 56, namely, 0.16 dex for stellar mass and 0.28 dex for the SFR. The inferred stellar mass and SFR were $3.7^{+2.6}_{-2.2} \times 10^{11}\,M_\odot$ and $2.5^{+7.5}_{-2.1} \times 10^2\,M_\odot$ yr^{-1}, respectively. By comparison, from the Hα fluxes contained with the three NIRSpec slits, an SFR of about $1.5 \times 10^2\,M_\odot$ yr^{-1} (before dust correction) was estimated. We noticed, however, that the slits only covered about 20% of the galaxy.

We examined systematic uncertainties of the stellar mass due to the presence of the faint AGN in the centre. First, we put an upper limit to its potential contribution to the integrated galaxy fluxes by means of aperture photometry. Specifically, we measured the fluxes in the HST and JWST filters from within 0.3 arcsec of the galaxy centre, where most of the AGN emission was expected according to the PSFs. We found that this region contributes less than 1% and 15% of the total galaxy light in the HST and JWST filters, respectively, which justifies that the AGN has only minor contributions in the rest-frame ultraviolet-to-optical. Second, we performed annulus-by-annulus spatially resolved SED fitting with Prospector using the HST and JWST data. With identical fitting set-ups as described above and conservatively excluding the $r < 0.3$ arcsec region, we found that the resulting mass decreases by only 0.08 dex with respect to the value from the integrated fitting above (Supplementary Fig. 1c,d). Such a decrease is negligible compared with the stellar mass uncertainty (0.3 dex) reported above, and thus we concluded that the AGN has no significant impact on mass measurements. The mass profile in Supplementary Fig. 1c appears to have small variations from a perfectly smooth disk profile (dashed line) by ±0.2 dex, which are, however, within the error bars. These features are also commonly found with comparable amplitudes in other disk galaxies at $z = 0$, including apparently isolated sources[49,57].

We also compared the best-fit parameter values with those inferred with a parametric SFH in a delayed exponentially declining form, which was adopted for stellar mass measurements by the majority of observational studies included in Fig. 3. The SED fit was conducted using the code CIGALE[58–60]. It models both the flux densities in the optical and infrared and the flux densities in the X-ray, the latter being measured with Chandra, based on the prescriptions described in ref. 61. The fitting assumptions were similar to those adopted for Prospector, except for the SFH[2]. According to the fitting results in Supplementary Fig. 2, the AGN emission (orange curve) had only minimal contribution ($\lesssim 10^{-3}$) to the observed fluxes (filled circles) in the optical and infrared filters. The best-fit stellar mass and SFR (averaged over 100 Myr) are $2.3^{+1.4}_{-0.9} \times 10^{11}\,M_\odot$ and $1.2^{+1.2}_{-0.6} \times 10^2\,M_\odot$ yr^{-1}, respectively, which are both within the uncertainty ranges inferred with Prospector.

Comparison sample of disk galaxies from the literature

Disk galaxies at $z = 3$–4 from the literature that were confirmed by kinematics and measured for size are included in Fig. 3a. They are from ground-based studies based on rest-frame optical emission lines[62–65], except for two objects that are based on the CO emission lines with ALMA[66] and optical emission lines with JWST[67]. All the disk galaxies were selected to have rotational velocities greater than the velocity dispersions, that is, $v_{rot} > \sigma_{int}$, which is a lenient disk criterion commonly adopted in the literature[7,9,68,69]. The stellar masses of all the disk galaxies were inferred using a Chabrier[54] or Kroupa IMF[70], except for the AMAZE[71] subsample in ref. 62, which adopts a Salpeter IMF[72].

We adjusted the latter to the Chabrier IMF by subtracting the reported mass values by 0.24 dex (refs. 73,74). We note that disks have also been identified kinematically beyond $z = 4$, which are not included in Fig. 3. These kinematically confirmed disks were mostly discovered with ALMA, whereas one was discovered with JWST[75–89]. The largest galaxies reported by these studies are around 5 kpc in radius[78,88], which is approximately two times smaller than the Big Wheel galaxy.

We note that kinematical measurements are essential for the confirmation of morphological disks, which have been discovered in the early epochs by recent JWST studies[90,91]. This is because measurements using imaging data alone may be subject to ambiguity of interpretation due to clumps, mergers, dust and peculiar galaxy geometry, all of which are commonly found at $z \gtrsim 1$ (refs. 9,92–94). As evidence supporting this argument, we examined the galaxies from ref. 43 at $z = 3$–4 with large radii (>0.5 arcsec) measured from HST near-infrared images and we found that the majority of them, if not all, have irregular or major merger-like, rather than disk-like, morphology. For this reason, only galaxies with kinematic measurements were considered for comparison in Fig. 3a.

Other measurements from the literature used for comparison

The size–mass scaling relationships in Fig. 3b were measured at or around the rest-frame 0.5 μm, which is the same wavelength where the size of the Big Wheel galaxy is measured. We included only star-forming galaxies[19,20,25,26,44,95]. The size–mass relationship of Ward et al.[19] was measured in two redshift bins, $z = 2$–3 and $z = 3$–5.5, and we adopted the average values to match the redshift of our galaxy ($z = 3.245$). The size–mass relationship of Costantin et al.[25] was provided as an analytical function of redshift and we adopted the relationship at $z = 3.2$. The size–mass relationship of Mowla et al.[44] was determined in the work as the median trend of a statistical galaxy sample at $z = 0.1$–0.5.

Based on the literature measurements, the probability of finding a star-forming galaxy, independent of kinematical confirmation, with the size of the Big Wheel at its stellar mass and redshift in random fields was obtained as follows. First, we calculated the expected galaxy size at the mass and redshift of the Big Wheel, using the relationships from two most recent and complete JWST studies[19,20], as shown in Fig. 3b. We found it to be 0.41 dex and 0.70 dex smaller than the observed size of the Big Wheel in logarithms using the relationships from ref. 19 and ref. 20, respectively. The distribution of sizes was well constrained as a log-normal in these studies with an intrinsic log-normal scatter in exponential units ($\sigma_{\log(R_e)}$) of these size–mass relationships of 0.22 dex and 0.28 dex, respectively. Therefore, the corresponding probabilities of finding a galaxy equal to or larger than the Big Wheel in random fields are 2% and 0.6% according to the two studies, respectively.

In addition, star-forming galaxies with masses larger than $10^{11}\,M_\odot$, such as the Big Wheel (which has a mass of at least $10^{11}\,M_\odot$), are extremely rare, independent of their sizes. This can be quantified again by using the previously quoted JWST results[19,20]. Only two star-forming galaxies with a mass greater than $10^{11}\,M_\odot$ have been detected in these surveys above $z = 3$ over a combined area of 440 arcmin^2 and no galaxies having a mass greater than $10^{11}\,M_\odot$, which is the lower limit for the Big Wheel considering different methodologies.

Thus, to randomly discover a galaxy with a mass of at least $10^{11}\,M_\odot$ at $z > 3$ and at sizes similar to the Big Wheel (using the conservative probability limit of 2%), if the environment does not play a role, we would have required a survey with a size of at least 11,000 arcmin^2.

The general galaxy population shown in Fig. 3c was selected to be at $z = 3.0$–3.5 from refs. 74,96. In the same panel, scaling relationships from two other literature studies[97,98] are also shown. The $z \approx 3.5$ galaxies in Fig. 3d were selected to have $v_{\rm rot}$ greater than $\sigma_{\rm int}$. We inferred their $v_{\rm circ}$ by performing a correction for disordered motions to $v_{\rm rot}$, which was measured at twice the half-light radius[64], following the same equation as used for the Big Wheel above. The $z \approx 0$ galaxies in the same panel are from ref. 14 and ref. 5. The stellar masses in these studies were all inferred assuming a Chabrier[54] IMF.

Data availability

The JWST data (Programme ID: General Observer 1835) are publicly available at https://mast.stsci.edu/search/ui/#/jwst. The HST data (Programme ID: 17065) are publicly available at https://mast.stsci.edu/search/ui/#/hst. The VLT HAWKI data (Programme ID: 110.23ZX) are publicly available at https://archive.eso.org/. The Chandra dataset (Programme ID: 23700358) is publicly available at https://cda.harvard.edu/chaser. The ALMA dataset ADS/JAO.ALMA#2021.1.00793.S. can be openly obtained at http://almascience.nao.ac.jp.

Code availability

The Source Extractor code is available at https://astromatic.github.io/sextractor/. The statmorph package is available at https://github.com/vrodgom/statmorph/. The emcee package is available at https://emcee.readthedocs.io/en/stable/. The galpy package is available at https://github.com/jobovy/galpy. The prospector code is available at https://github.com/bd-j/prospector. The CIGALE code is available at https://cigale.lam.fr/. The drizzle code is available to download at https://github.com/spacetelescope/drizzle. The JWST pipeline is available at https://github.com/spacetelescope/jwst. The Common Astronomy Software Application (CASA) is available at https://casa.nrao.edu/. The WEBBPSF code is available at https://github.com/spacetelescope/webbpsf.

References

1. Pensabene, A. et al. ALMA survey of a massive node of the Cosmic Web at $z \sim 3$. I. Discovery of a large overdensity of CO emitters. *Astron. Astrophys.* **684**, A119 (2024).
2. Galbiati, M. et al. Connecting the growth of galaxies to the large-scale environment in a massive node of the Cosmic Web at $z \sim 3$. Preprint at https://arxiv.org/abs/2410.03822 (2024).
3. Gil de Paz, A. et al. The GALEX ultraviolet atlas of nearby galaxies. *Astrophys. J. Suppl. Ser.* **173**, 185–255 (2007).
4. Rodriguez-Gomez, V. et al. The optical morphologies of galaxies in the IllustrisTNG simulation: a comparison to Pan-STARRS observations. *Mon. Not. R. Astron.* **483**, 4140–4159 (2019).
5. Lelli, F., McGaugh, S. S. & Schombert, J. M. SPARC: mass models for 175 disk galaxies with Spitzer photometry and accurate rotation curves. *Astron. J.* **152**, 157 (2016).
6. Foreman-Mackey, D., Hogg, D. W., Lang, D. & Goodman, J. emcee: the MCMC hammer. *Publ. Astron. Soc. Pac.* **125**, 306–312 (2013).
7. Kassin, S. A. et al. The epoch of disk settling: $z \sim 1$ to now. *Astrophys. J.* **758**, 106 (2012).
8. Law, D. R. et al. High velocity dispersion in a rare grand-design spiral galaxy at redshift $z = 2.18$. *Nature* **487**, 338–340 (2012).
9. Förster Schreiber, N. M. & Wuyts, S. Star-forming galaxies at cosmic noon. *Annu. Rev. Astron. Astrophys.* **58**, 661–725 (2020).
10. Übler, H. et al. The evolution of the Tully–Fisher relation between $z \sim 2.3$ and $z \sim 0.9$ with KMOS^{3D}. *Astrophys. J.* **842**, 121 (2017).
11. Leja, J., Johnson, B. D., Conroy, C., van Dokkum, P. G. & Byler, N. Deriving physical properties from broadband photometry with Prospector: description of the model and a demonstration of its accuracy using 129 galaxies in the local Universe. *Astrophys. J.* **837**, 170 (2017).
12. Nanayakkara, T. et al. A population of faint, old, and massive quiescent galaxies at $3 < z < 4$ revealed by JWST NIRSpec spectroscopy. *Sci. Rep.* **14**, 3724 (2024).
13. Ogle, P. M., Lanz, L., Nader, C. & Helou, G. Superluminous spiral galaxies. *Astrophys. J.* **817**, 109 (2016).
14. Di Teodoro, E. M., Posti, L., Ogle, P. M., Fall, S. M. & Jarrett, T. Rotation curves and scaling relations of extremely massive spiral galaxies. *Mon. Not. R. Astron.* **507**, 5820–5831 (2021).
15. Mo, H. J., Mao, S. & White, S. D. M. The formation of galactic discs. *Mon. Not. R. Astron.* **295**, 319–336 (1998).
16. Bullock, J. S. et al. A universal angular momentum profile for galactic halos. *Astrophys. J.* **555**, 240–257 (2001).

17. Bryan, S. E. et al. The impact of baryons on the spins and shapes of dark matter haloes. *Mon. Not. R. Astron.* **429**, 3316–3329 (2013).
18. Zjupa, J. & Springel, V. Angular momentum properties of haloes and their baryon content in the Illustris simulation. *Mon. Not. R. Astron.* **466**, 1625–1647 (2017).
19. Ward, E. et al. Evolution of the size–mass relation of star-forming galaxies since z=5.5 revealed by CEERS. *Astrophys. J.* **962**, 176 (2024).
20. Varadaraj, R. G. et al. The sizes of bright Lyman-break galaxies at z=3-5 with JWST PRIMER. *Mon. Not. R. Astron.* **533**, 3724–3741 (2024).
21. Jian, H.-Y., Lin, L. & Chiueh, T. Environmental dependence of the galaxy merger rate in a ΛCDM universe. *Astrophys. J.* **754**, 26 (2012).
22. Governato, F. et al. Forming a large disc galaxy from a z<1 major merger. *Mon. Not. R. Astron.* **398**, 312–320 (2009).
23. Hopkins, P. F., Cox, T. J., Younger, J. D. & Hernquist, L. How do disks survive mergers? *Astrophys. J.* **691**, 1168–1201 (2009).
24. Stewart, K. R. et al. High angular momentum halo gas: a feedback and code-independent prediction of LCDM. *Astrophys. J.* **843**, 47 (2017).
25. Costantin, L. et al. Expectations of the size evolution of massive galaxies at $3 \leq z \leq 6$ from the TNG50 simulation: the CEERS/JWST view. *Astrophys. J.* **946**, 71 (2023).
26. LaChance, P. et al. The evolution of galaxy morphology from redshift z=6 to 3: mock JWST observations of galaxies in the ASTRID simulation. Preprint at https://arxiv.org/abs/2401.16608 (2024).
27. Bushouse, H. et al. JWST Calibration Pipeline v.1.8.0 (2022).
28. Bagley, M. B. et al. CEERS epoch 1 NIRCam imaging: reduction methods and simulations enabling early JWST science results. *Astrophys. J. Lett.* **946**, L12 (2023).
29. ESO CPL Development Team. EsoRex: ESO recipe execution tool. *Astrophysics Source Code Library* ascl:1504.003 (2015).
30. Bertin, E. & Arnouts, S. SExtractor: software for source extraction. *Astron. Astrophys. Suppl.* **117**, 393–404 (1996).
31. Fruchter, A. S. & Hook, R. N. Drizzle: a method for the linear reconstruction of undersampled images. *Publ. Astron. Soc. Pac.* **114**, 144–152 (2002).
32. Perrin, M. D. et al. Updated point spread function simulations for JWST with WebbPSF. In *Space Telescopes and Instrumentation 2014: Optical, Infrared, and Millimeter Wave* (eds Oschmann, J. et al.) Vol. 9143, 91433X (SPIE, 2014).
33. CASA Team et al. CASA, the common astronomy software applications for radio astronomy. *Publ. Astron. Soc. Pac.* **134**, 114501 (2022).
34. Travascio, A. et al. X-ray view of a massive node of the Cosmic Web at z~3 I. An exceptional overdensity of rapidly accreting supermassive black holes. *Astro. Astrophys.* **694**, A165 (2025).
35. Ueda, Y., Akiyama, M., Hasinger, G., Miyaji, T. & Watson, M. G. Toward the standard population synthesis model of the X-ray background: evolution of X-ray luminosity and absorption functions of active galactic nuclei including Compton-thick populations. *Astrophys. J.* **786**, 104 (2014).
36. Kewley, L. J., Dopita, M. A., Sutherland, R. S., Heisler, C. A. & Trevena, J. Theoretical modeling of starburst galaxies. *Astrophys. J.* **556**, 121–140 (2001).
37. Baldwin, J. A., Phillips, M. M. & Terlevich, R. Classification parameters for the emission-line spectra of extragalactic objects. *Publ. Astron. Soc. Pac.* **93**, 5–19 (1981).
38. Sérsic, J. L. Influence of the atmospheric and instrumental dispersion on the brightness distribution in a galaxy. *Bol. Asoc. Argent. Astron. Plata Argent.* **6**, 41–43 (1963).
39. Domínguez, A. et al. Dust extinction from Balmer decrements of star-forming galaxies at $0.75 \leqslant z \leqslant 1.5$ with Hubble Space Telescope/Wide-Field-Camera 3 spectroscopy from the WFC3 Infrared Spectroscopic Parallel Survey. *Astrophys. J.* **763**, 145 (2013).
40. D'Eugenio, F. et al. JADES Data Release 3 – NIRSpec/MSA spectroscopy for 4,000 galaxies in the GOODS fields. Preprint at https://arxiv.org/abs/2404.06531 (2024).
41. Calzetti, D. The dust opacity of star-forming galaxies. *Publ. Astron. Soc. Pac.* **113**, 1449–1485 (2001).
42. Nelson, E. J. et al. Millimeter mapping at z~1: dust-obscured bulge building and disk growth. *Astrophys. J.* **870**, 130 (2019).
43. van der Wel, A. et al. 3D-HST+CANDELS: the evolution of the galaxy size–mass distribution since z=3. *Astrophys. J.* **788**, 28 (2014).
44. Mowla, L. A. et al. COSMOS-DASH: the evolution of the galaxy size–mass relation since z~3 from new wide-field WFC3 imaging combined with CANDELS/3D-HST. *Astrophys. J.* **880**, 57 (2019).
45. Bovy, J. galpy: a python library for galactic dynamics. *Astrophys. J. Suppl. Ser.* **216**, 29 (2015).
46. Burkert, A. The structure of dark matter halos in dwarf galaxies. *Astrophys. J. Lett.* **447**, L25–L28 (1995).
47. Rubin, V. C., Ford Jr, W. K. & Thonnard, N. Extended rotation curves of high-luminosity spiral galaxies. IV. Systematic dynamical properties, Sa → Sc. *Astrophys. J. Lett.* **225**, L107–L111 (1978).
48. Noordermeer, E., van der Hulst, J. M., Sancisi, R., Swaters, R. S. & van Albada, T. S. The mass distribution in early-type disc galaxies: declining rotation curves and correlations with optical properties. *Mon. Not. R. Astron.* **376**, 1513–1546 (2007).
49. de Blok, W. J. G. et al. High-resolution rotation curves and galaxy mass models from THINGS. *Astron. J.* **136**, 2648–2719 (2008).
50. Nestor Shachar, A. et al. RC100: rotation curves of 100 massive star-forming galaxies at z=0.6–2.5 reveal little dark matter on galactic scales. *Astrophys. J.* **944**, 78 (2023).
51. Weiner, B. J. et al. A survey of galaxy kinematics to z~1 in the TKRS/GOODS-N field. I. Rotation and dispersion properties. *Astrophys. J.* **653**, 1027–1048 (2006).
52. Johnson, B. D., Leja, J., Conroy, C. & Speagle, J. S. Stellar population inference with Prospector. *Astrophys. J. Suppl. Ser.* **254**, 22 (2021).
53. Wang, B. et al. The UNCOVER survey: a first-look HST+JWST catalog of galaxy redshifts and stellar population properties spanning $0.2 \lesssim z \lesssim 15$. *Astrophys. J. Suppl. Ser.* **270**, 12 (2024).
54. Chabrier, G. Galactic stellar and substellar initial mass function. *Publ. Astron. Soc. Pac.* **115**, 763–795 (2003).
55. Charlot, S. & Fall, S. M. A simple model for the absorption of starlight by dust in galaxies. *Astrophys. J.* **539**, 718–731 (2000).
56. Pacifici, C. et al. The art of measuring physical parameters in galaxies: a critical assessment of spectral energy distribution fitting techniques. *Astrophys. J.* **944**, 141 (2023).
57. Lange, R. et al. Galaxy and mass assembly (GAMA): mass–size relations of z<0.1 galaxies subdivided by Sérsic index, colour and morphology. *Mon. Not. R. Astron.* **447**, 2603–2630 (2015).
58. Burgarella, D., Buat, V. & Iglesias-Páramo, J. Star formation and dust attenuation properties in galaxies from a statistical ultraviolet-to-far-infrared analysis. *Mon. Not. R. Astron.* **360**, 1413–1425 (2005).
59. Noll, S. et al. Analysis of galaxy spectral energy distributions from far-UV to far-IR with CIGALE: studying a SINGS test sample. *Astron. Astrophys.* **507**, 1793–1813 (2009).
60. Boquien, M. et al. CIGALE: a python Code Investigating GALaxy Emission. *Astron. Astrophys.* **622**, A103 (2019).
61. Yang, G. et al. Fitting AGN/Galaxy X-ray-to-radio SEDs with CIGALE and improvement of the code. *Astrophys. J.* **927**, 192 (2022).
62. Gnerucci, A. et al. Dynamical properties of AMAZE and LSD galaxies from gas kinematics and the Tully–Fisher relation at z~3. *Astron. Astrophys.* **528**, A88 (2011).
63. Livermore, R. C. et al. Resolved spectroscopy of gravitationally lensed galaxies: global dynamics and star-forming clumps on ~100 pc scales at $1 < z < 4$. *Mon. Not. R. Astron.* **450**, 1812–1835 (2015).

64. Turner, O. J. et al. The KMOS Deep Survey (KDS): I. Dynamical measurements of typical star-forming galaxies at $z=3.5$. *Mon. Not. R. Astron.* **471**, 1280–1320 (2017).
65. Gillman, S. et al. The dynamics and distribution of angular momentum in HiZELS star-forming galaxies at $z=0.8$-3.3. *Mon. Not. R. Astron.* **486**, 175–194 (2019).
66. Swinbank, A. M. et al. ALMA resolves the properties of star-forming regions in a dense gas disk at $z\sim3$. *Astrophys. J. Lett.* **806**, L17 (2015).
67. Wu, Y. et al. The identification of a dusty multiarm spiral galaxy at $z=3.06$ with JWST and ALMA. *Astrophys. J. Lett.* **942**, L1 (2023).
68. Simons, R. C. et al. $z\sim2$: an epoch of disk assembly. *Astrophys. J.* **843**, 46 (2017).
69. Wisnioski, E. et al. The KMOS^{3D} survey: design, first results, and the evolution of galaxy kinematics from $0.7\leqslant z\leqslant2.7$. *Astrophys. J.* **799**, 209 (2015).
70. Kroupa, P. On the variation of the initial mass function. *Mon. Not. R. Astron.* **322**, 231–246 (2001).
71. Maiolino, R. et al. AMAZE. I. The evolution of the mass-metallicity relation at $z>3$. *Astron. Astrophys.* **488**, 463–479 (2008).
72. Salpeter, E. E. The luminosity function and stellar evolution. *Astrophys. J.* **121**, 161 (1955).
73. Courteau, S. et al. Galaxy masses. *Rev. Mod. Phys.* **86**, 47–119 (2014).
74. Santini, P. et al. Stellar masses from the CANDELS survey: the GOODS-South and UDS fields. *Astrophys. J.* **801**, 97 (2015).
75. Carniani, S. et al. Strongly star-forming rotating disks in a complex merging system at $z=4.7$ as revealed by ALMA. *Astron. Astrophys.* **559**, A29 (2013).
76. Jones, G. C. et al. Dynamical characterization of galaxies at $z\sim4$–6 via tilted ring fitting to ALMA [C II] observations. *Astrophys. J.* **850**, 180 (2017).
77. Tadaki, K. et al. The gravitationally unstable gas disk of a starburst galaxy 12 billion years ago. *Nature* **560**, 613–616 (2018).
78. Neeleman, M., Kanekar, N., Prochaska, J. X., Rafelski, M. A. & Carilli, C. L. [C II] 158 μm emission from $z\sim4$ H I absorption-selected galaxies. *Astrophys. J. Lett.* **870**, L19 (2019).
79. Rizzo, F. et al. A dynamically cold disk galaxy in the early Universe. *Nature* **584**, 201–204 (2020).
80. Rizzo, F., Vegetti, S., Fraternali, F., Stacey, H. R. & Powell, D. Dynamical properties of $z=4.5$ dusty star-forming galaxies and their connection with local early-type galaxies. *Mon. Not. R. Astron.* **507**, 3952–3984 (2021).
81. Rizzo, F. et al. The ALMA-ALPAKA survey. I. High-resolution CO and [CI] kinematics of star-forming galaxies at $z=0.5$-3.5. *Astron. Astrophys.* **679**, A129 (2023).
82. Fraternali, F. et al. Fast rotating and low-turbulence discs at $z=4.5$: dynamical evidence of their evolution into local early-type galaxies. *Astron. Astrophys.* **647**, A194 (2021).
83. Fujimoto, S. et al. ALMA lensing cluster survey: bright [C II] 158 μm lines from a multiply imaged sub-L* galaxy at $z=6.0719$. *Astrophys. J.* **911**, 99 (2021).
84. Lelli, F. et al. A massive stellar bulge in a regularly rotating galaxy 1.2 billion years after the Big Bang. *Science* **371**, 713–716 (2021).
85. Tsukui, T. & Iguchi, S. Spiral morphology in an intensely star-forming disk galaxy more than 12 billion years ago. *Science* **372**, 1201–1205 (2021).
86. Herrera-Camus, R. et al. Kiloparsec view of a typical star-forming galaxy when the Universe was ~1 Gyr old. II. Regular rotating disk and evidence for baryon dominance on galactic scales. *Astron. Astrophys.* **665**, L8 (2022).
87. Nelson, E. J. et al. JWST reveals a population of ultrared, flattened galaxies at $2\lesssim z\lesssim6$ previously missed by HST. *Astrophys. J. Lett.* **948**, L18 (2023).
88. Parlanti, E. et al. ALMA hints at the presence of turbulent disk galaxies at $z>5$. *Astron. Astrophys.* **673**, A153 (2023).
89. Roman-Oliveira, F., Fraternali, F. & Rizzo, F. Regular rotation and low turbulence in a diverse sample of $z=4.5$ galaxies observed with ALMA. *Mon. Not. R. Astron.* **521**, 1045–1065 (2023).
90. Ferreira, L. et al. Panic! at the disks: first rest-frame optical observations of galaxy structure at $z>3$ with JWST in the SMACS 0723 field. *Astrophys. J. Lett.* **938**, L2 (2022).
91. Ferreira, L. et al. The JWST Hubble sequence: the rest-frame optical evolution of galaxy structure at $1.5<z<6.5$. *Astrophys. J.* **955**, 94 (2023).
92. van der Wel, A. et al. Geometry of star-forming galaxies from SDSS, 3D-HST, and CANDELS. *Astrophys. J. Lett.* **792**, L6 (2014).
93. Guo, Y. et al. Clumpy galaxies in CANDELS. I. The definition of UV clumps and the fraction of clumpy galaxies at $0.5<z<s3$. *Astrophys. J.* **800**, 39 (2015).
94. Vega-Ferrero, J. et al. On the nature of disks at high redshift seen by JWST/CEERS with contrastive learning and cosmological simulations. *Astrophys. J.* **961**, 51 (2024).
95. Ormerod, K. et al. EPOCHS VI: the size and shape evolution of galaxies since $z\sim8$ with JWST observations. *Mon. Not. R. Astron.* **527**, 6110–6125 (2024).
96. Barro, G. et al. The CANDELS/SHARDS multiwavelength catalog in GOODS-N: photometry, photometric redshifts, stellar masses, emission-line fluxes, and star formation rates. *Astrophys. J. Suppl. Ser.* **243**, 22 (2019).
97. Speagle, J. S., Steinhardt, C. L., Capak, P. L. & Silverman, J. D. A highly consistent framework for the evolution of the star-forming 'main sequence' from $z\sim0$-6. *Astrophys. J. Suppl. Ser.* **214**, 15 (2014).
98. Popesso, P. et al. The main sequence of star-forming galaxies across cosmic times. *Mon. Not. R. Astron.* **519**, 1526–1544 (2023).

Acknowledgements

We thank B. Wang, P. Madau, M. Dotti, A. de la Vega, Y. Guo, C. Bacchini, Z. Cai, C. Conselice, A. Dekel, S. Faber, F. Fraternali, L. Ho, F. Jiang, S. Kassin, D. Koo, N. Mandelker, S. Mao and D. Xu for the valuable and insightful discussions regarding the research topics relevant to this paper. This project was supported by the European Research Council (ERC) Consolidator Grant no. 864361 (CosmicWeb). A.P. acknowledges the support from Fondazione Cariplo grant no. 2020-0902. M.V.M. acknowledges funding from NASA by means of HST-GO-17065. T.N. acknowledges support from Australian Research Council Laureate Fellowship FL180100060. This work is based in part on observations made with the NASA/ESA/CSA James Webb Space Telescope. The data were obtained from the Mikulski Archive for Space Telescopes at the Space Telescope Science Institute, which is operated by the Association of Universities for Research in Astronomy, Inc., under NASA contract NAS 5-03127 for JWST. These observations are associated with programme no. 1835. Support for programme no. 1835 was provided by NASA through a grant from the Space Telescope Science Institute, which is operated by the Association of Universities for Research in Astronomy, Inc., under NASA contract NAS 5-03127. This research is based on observations made with the NASA/ESA Hubble Space Telescope obtained from the Space Telescope Science Institute, which is operated by the Association of Universities for Research in Astronomy, Inc., under NASA contract NAS 5-26555. These observations are associated with programme 17065. ALMA is a partnership of ESO (representing its member states), NSF (USA) and NINS (Japan), together with NRC (Canada), MOST and ASIAA (Taiwan), and KASI (Republic of Korea), in cooperation with the Republic of Chile. The Joint ALMA Observatory is operated by ESO, AUI/NRAO and NAOJ. The scientific results reported in this article are based in part on observations made by the Chandra X-ray Observatory. This work is also based on observations collected at the European Southern Observatory under ESO programme 110.23ZX.

Author contributions

W.W. was responsible for the JWST and HST observations, reducing the data from JWST, HST and VLT, conducting the imaging, spectroscopic and modelling analyses of this work, and producing the figures. W.W. also worked in collaboration with S.C. to write the text. S.C. led the proposal and planning for the JWST, HST and VLT observations used in this work, and contributed to the observational and theoretical analyses and interpretation of the data, and to the writing of the text. A.P. was responsible for the ALMA observations, conducted the analysis and modelling of ALMA data, and contributed to the interpretation and discussion. M.G. contributed to the observation planning, assisted in reducing the VLT data, performed the SED fitting and contributed to the interpretation of the results. A.T. planned the Chandra observations, reduced the Chandra data and contributed to analyses relevant to the AGN properties. C.C.S. assisted with the JWST target selection, observation planning and data reduction, and contributed to the interpretation of science results. M. Fossati and M. Fumagalli assisted with the JWST proposal preparation and contributed to the interpretation and discussion of the observational results. T.L., S.d.B. and G.Q. contributed to the comparison with simulations and relevant discussion. M.V.M. assisted with the JWST NIRSpec MSA mask design and preparation of the APT files, advised on observing and data reduction strategies, and contributed to the interpretation and discussion. S.G.G., J.M., R.M., T.N. and G.P. contributed to the proposal planning, data interpretation and discussion for the JWST and HST observations.

Competing interests

The authors declare no competing interests.

Additional information

Extended data is available for this paper at https://doi.org/10.1038/s41550-025-02500-2.

Supplementary information The online version contains supplementary material available at https://doi.org/10.1038/s41550-025-02500-2.

Correspondence and requests for materials should be addressed to Weichen Wang.

https://doi.org/10.1038/s41550-025-02500-2

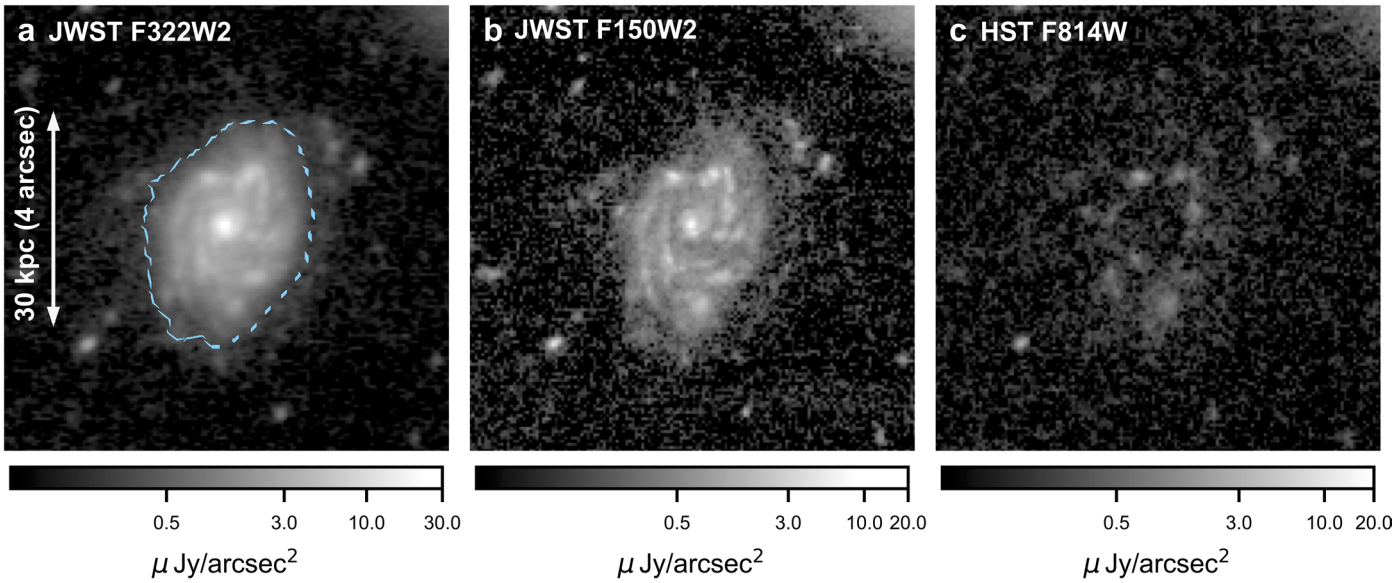

Extended Data Fig. 1 | Galaxy images in the JWST near-infrared filters and the HST optical filter. Colorbars at the bottom indicate the observed surface brightness. The contour in a represents the 5-σ isophote demarcating the full detected extent of the galaxy, which reaches more than 30 kiloparsecs. The galaxy disk is detected in the two near-infrared filters (**a**, **b**), while only a few clumps are detected in the HST filter (**c**).

https://doi.org/10.1038/s41550-025-02500-2

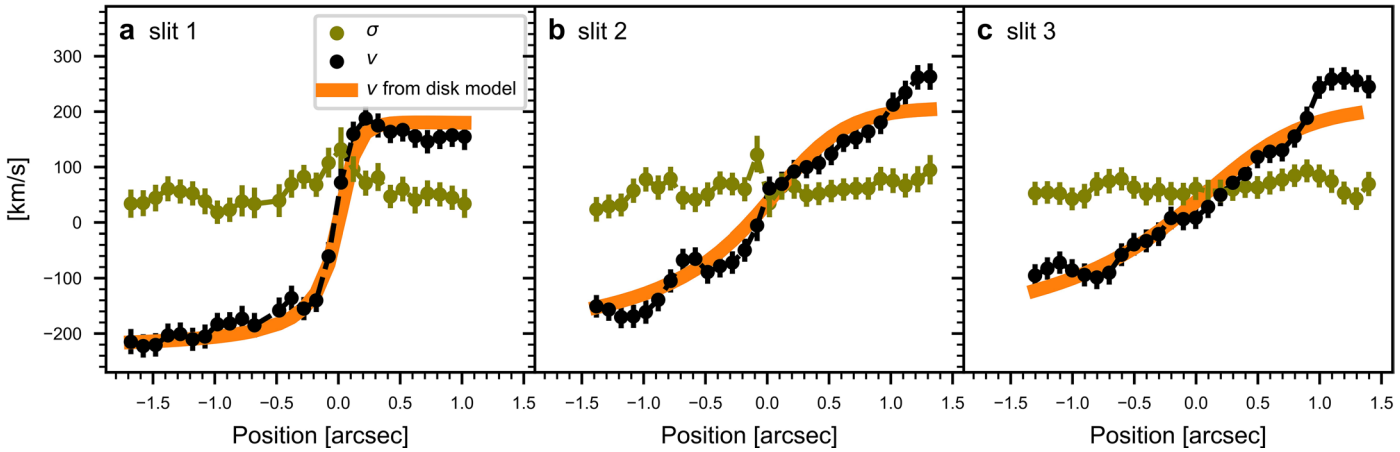

Extended Data Fig. 2 | The line-of-sight rotational velocity (v) and velocity dispersion (σ) profiles measured from three slits, along with the disk model predictions. a–**c**, The profiles for slit 1 (**a**), slit 2 (**b**) and slit 3 (**c**). The X axis of each panel indicates the spatial location along a slit where the v and σ are measured. Although deviations exist, the disk model captures the bulk trends of the observed v profiles remarkably well, justifying that the ionized gas of the galaxy is predominantly in the ordered motion expected for a disk. Errorbars represent 1-σ uncertainties.

https://doi.org/10.1038/s41550-025-02500-2

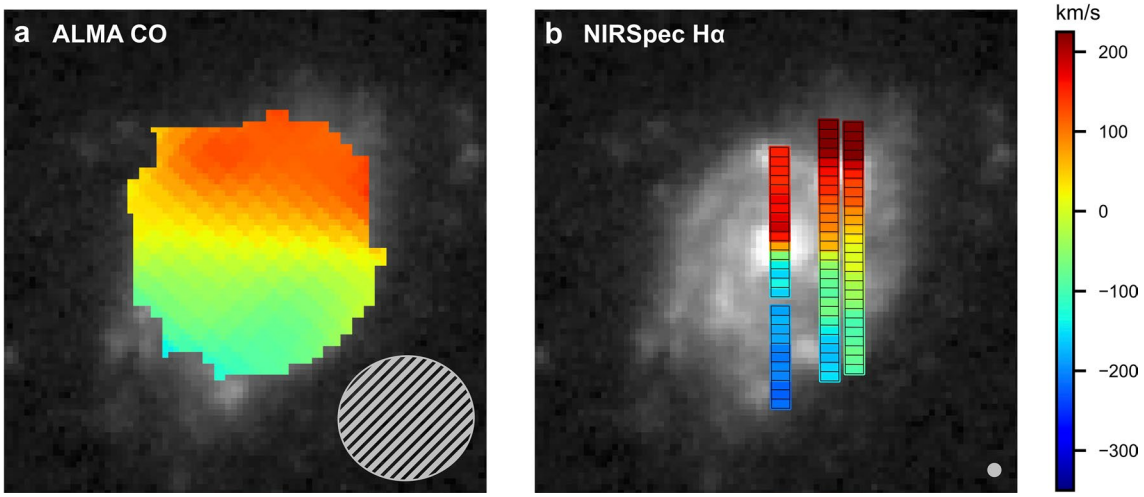

Extended Data Fig. 3 | The galaxy velocity map measured from the CO and Hα spectral lines. The values of the line-of-sight velocities are indicated by the colorbar, and the PSFs (in FWHM) of the data are indicated at the lower right corners of the two panels. The CO map (**a**) has a substantially larger PSF than the Hα map (**b**) and, as a result, shows narrower spans of velocity due to the beam-smearing effect[51]. Nevertheless, the CO map shows smooth velocity gradients oriented along the galaxy major axis similarly to the Hα map, providing additional evidence that the galaxy is consistent with a rotating disk.

https://doi.org/10.1038/s41550-025-02500-2

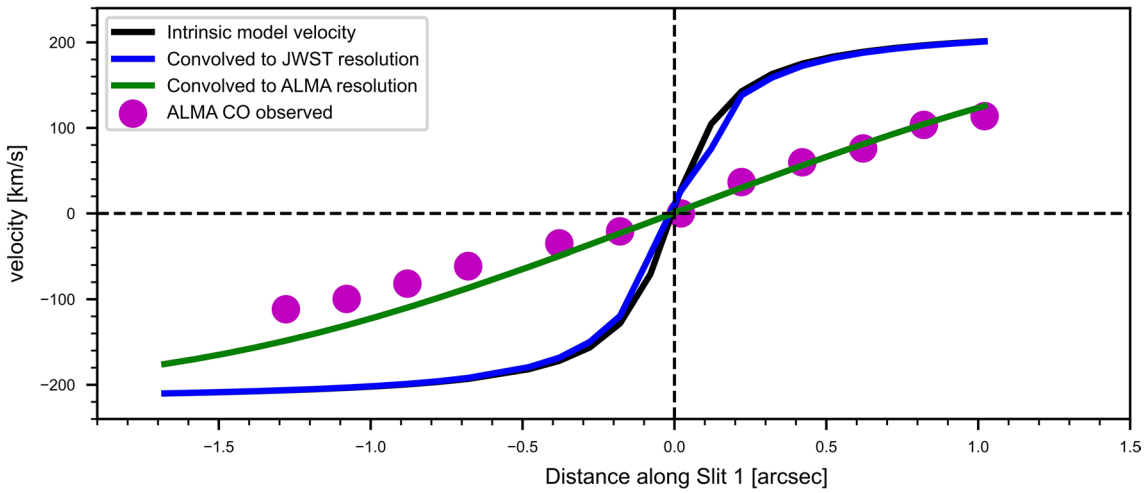

Extended Data Fig. 4 | Galaxy velocity profiles extracted from the 3D emission line models, which are created to examine the beam-smearing effects. The beam-smearing effect of JWST is found to have negligible impacts on the Hα velocity measurements thanks to the exquisite spatial resolution, as demonstrated by that the Hα velocity profile 'seen' at the JWST resolution (blue line) almost fully overlaps with the intrinsic profile (black line). Second, the Hα kinematics is found in overall agreement with the CO kinematics. This is demonstrated by that the Hα velocity profile 'seen' at the ALMA resolution (green line) matches the observed ALMA CO velocity profile (purple points). Refer to Methods for more details.

https://doi.org/10.1038/s41550-025-02500-2

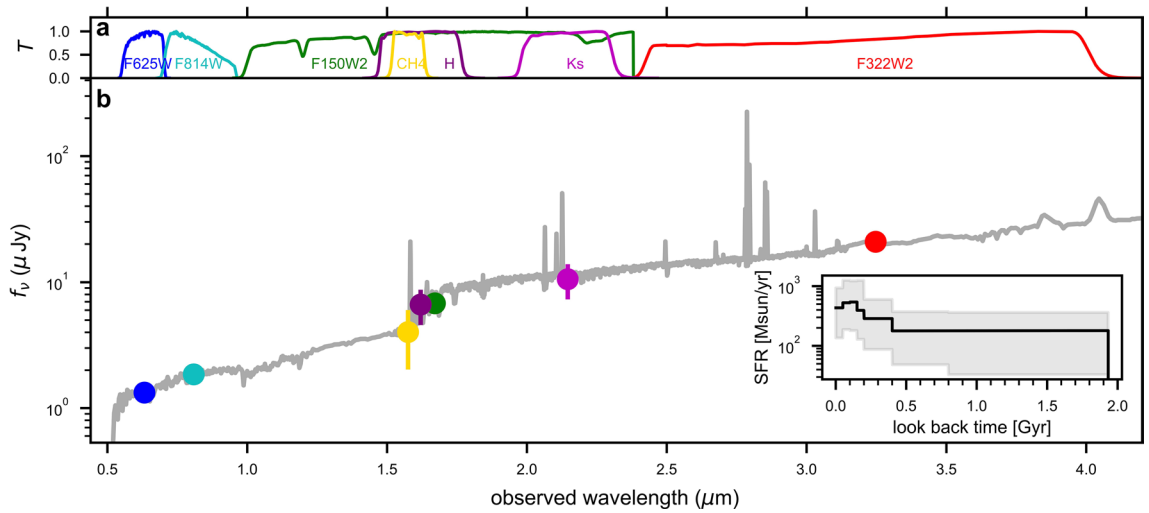

Extended Data Fig. 5 | The observed SED of the Big Wheel along with its best-fit model obtained with prospector. (**a**) Transmission curves of the photometric filters used in the observations are plotted as a function of wavelength. Each curve is normalized to its maximum. (**b**) The best-fit model (gray curve) is plotted along with the observed flux densities (points with 3-σ errorbars). For the observed flux densities, the value measured in a given filter is colored in the same way as in a. The vertical axis indicates the flux density. The best-fit star formation history is shown as the black line in the inset, and the gray shade indicates uncertainties.

https://doi.org/10.1038/s41550-025-02500-2

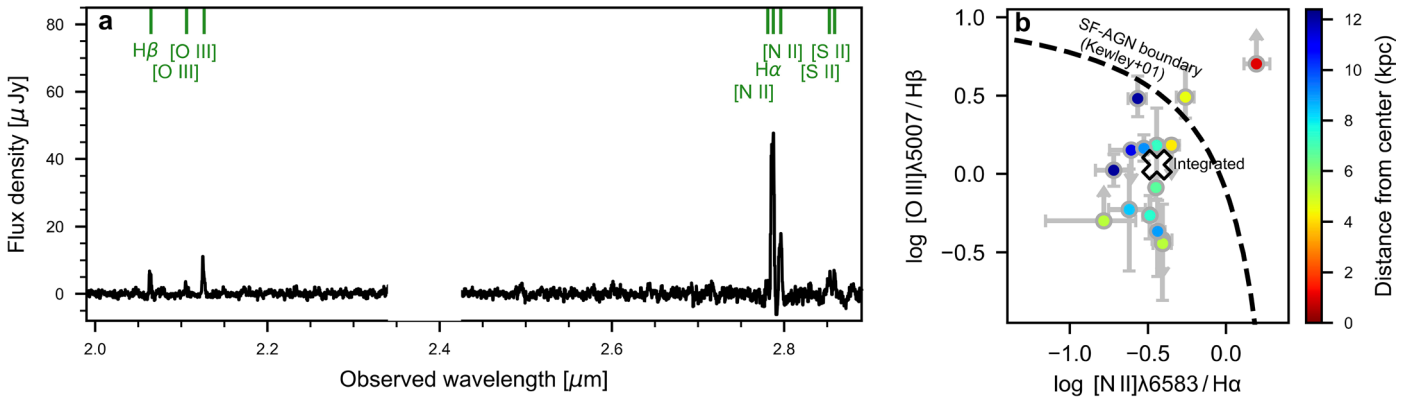

Extended Data Fig. 6 | The integrated galaxy spectrum and spatially resolved BPT diagram. (**a**) The galaxy is detected with multiple emission lines in the rest-frame optical, the observed wavelengths of which at the galaxy redshift (z = 3.245) are indicated in the figure. The spectral continuum has been subtracted. The break near the middle of the figure is caused by the gap between the JWST NIRSpec detectors. (**b**) The emission line ratios measured from individual parts of the galaxy within the NIRSpec slits are presented along with the integrated measurement, each color-coded by the distance from the galaxy center. Errorbars indicate 3-sigma uncertainties or detection limits. The dashed curve separates AGNs (toward upper right) from star-forming galaxies (toward lower right) and is adopted from Kewley et al.[36] Only the central part of the galaxy (r < 1.5 kpc) appears to be dominated by AGN-like emission.